Geosci. Instrum. Method. Data Syst., 6, 39–51, 2017
www.geosci-instrum-method-data-syst.net/6/39/2017/
doi:10.5194/gi-6-39-2017

Geoscientific Instrumentation Methods and Data Systems
Open Access
EGU

Radio-frequency interference mitigating hyperspectral L-band radiometer

Peter Toose[1], Alexandre Roy[2], Frederick Solheim[3], Chris Derksen[1], Tom Watts[4], Alain Royer[2], and Anne Walker[1]

[1]Climate Research Division, Environment and Climate Change Canada, Toronto, Ontario, M3H 5T4, Canada
[2]Centre d'Applications et de Recherches en Télédétection, Université de Sherbrooke, Sherbrooke, Québec, J1K 2R1, Canada
[3]Dakota Ridge Research and Development, Boulder, Colorado, 80303, USA
[4]Department of Geography, Northumbria University, Newcastle upon Tyne, NE1 8ST, UK

Correspondence to: Peter Toose (peter.toose@canada.ca)

Received: 6 July 2016 – Published in Geosci. Instrum. Method. Data Syst. Discuss.: 18 July 2016
Revised: 5 December 2016 – Accepted: 8 December 2016 – Published: 1 February 2017

Abstract. Radio-frequency interference (RFI) can significantly contaminate the measured radiometric signal of current spaceborne L-band passive microwave radiometers. These spaceborne radiometers operate within the protected passive remote sensing and radio-astronomy frequency allocation of 1400–1427 MHz but nonetheless are still subjected to frequent RFI intrusions. We present a unique surface-based and airborne hyperspectral 385 channel, dual polarization, L-band Fourier transform, RFI-detecting radiometer designed with a frequency range from 1400 through $\approx$ 1550 MHz. The extended frequency range was intended to increase the likelihood of detecting adjacent RFI-free channels to increase the signal, and therefore the thermal resolution, of the radiometer instrument. The external instrument calibration uses three targets (sky, ambient, and warm), and validation from independent stability measurements shows a mean absolute error (MAE) of 1.0 K for ambient and warm targets and 1.5 K for sky. A simple but effective RFI removal method which exploits the large number of frequency channels is also described. This method separates the desired thermal emission from RFI intrusions and was evaluated with synthetic microwave spectra generated using a Monte Carlo approach and validated with surface-based and airborne experimental measurements.

1 Introduction

A number of spaceborne L-band passive microwave radiometer missions were successfully launched in recent years for global monitoring of soil moisture and sea surface salinity. The European Space Agency Soil Moisture and Ocean Salinity (SMOS) mission (Kerr et al., 2010) was launched in November 2009 and continues to operate. The NASA Aquarius instrument on board the Argentine SAC-D spacecraft acquired L-band observations between September 2012 to July 2015 (Lagerloef et al., 2013), and the NASA Soil Moisture Active Passive (SMAP) satellite was launched in January 2015 (Entekhabi et al., 2015). In addition to monitoring soil moisture and sea surface salinity, these missions also provide useful measurements for cryospheric applications including monitoring the freeze–thaw state of the land surface (Rautiainen et al., 2016, 2014; Roy et al., 2015), estimating snow density and ground permittivity (Schwank et al., 2015; Lemmetyinen et al., 2016), and retrieving the thickness of thin sea ice (Kaleschke et al., 2016, 2012).

Even though the SMOS, Aquarius, and SMAP radiometer bandwidths fall within a protected band (1400–1427 MHz), significant levels of radio-frequency interference (RFI) caused by anthropogenic sources of radiation are commonly observed in satellite L-band measurements (Oliva et al., 2016; Le Vine et al., 2014; Piepmeier et al., 2014; Aksoy and Johnson, 2013). The United Nations provision 5.340 of Radio Regulations of the International Telecommunication Union Radiocommunication Sector (ITU-R) has regulated that the frequency allocation of 1400–1427 MHz be dedicated to passive remote sensing from space and radio-

astronomy research and that all other emissions within this band be prohibited or limited to maximum permitted emission power levels (ITU, 2012). Illegal sources, in addition to spurious and harmonic emissions and other unwarranted transmissions, often violate these reserved bands or exceed the maximum permitted emission power levels, producing RFI. The natural thermal emissions in these protected wavebands are orders of magnitude lower in power than active RFI sources; therefore, such RFI intrusions can contaminate and even blind the passive observations. A number of different hardware and processing approaches have been explored and implemented for handling RFI intrusions for a variety of L-band radiometer systems (Guner et al., 2007; Fanise et al., 2011; Forte et al., 2011; Pardé et al., 2011; Misra et al., 2009). The SMOS mission was the first L-band spaceborne mission launched in several decades and thus was the least prepared for dealing with the prevalence of RFI contamination. Anterrieu and Khazâal (2011) and Khazâal et al. (2014) developed post-launch methods to flag SMOS snapshots as RFI-contaminated by identifying outliers in temporally averaged Level L1a data and evaluating the kurtosis for each snapshot. These methods simply identify RFI-contaminated data with no mitigation applied and were developed specifically for SMOS due to the unique SMOS hardware and software architecture, which does not archive the radiometric signals at their highest temporal resolution, limiting standard approaches for detecting RFI contamination (Anterrieu and Khazâal, 2011). The prevalence of L-band RFI was acknowledged prior to the launch of the Aquarius instrument, and thus the radiometer was designed with RFI mitigating capabilities. Le Vine et al. (2014) describe the rapid sampling "glitch detection" algorithm employed by the Aquarius L-band instrument that differs from SMOS by rapidly sampling the scene many times in the time required for the antenna to move half the width of an image pixel, so that potentially those samples corrupted with RFI could be identified by comparing these measurements to preset thresholds. If the samples exceed the thresholds, they are flagged as RFI and are not included in computing the mean of all measured samples for an image pixel. The recently launched SMAP mission employs a more advanced RFI mitigation technology that was not available to previous generation spaceborne L-band radiometers, involving both space-flight instrument hardware and ground-based processing algorithms. Piepmeier et al. (2014) describe the hardware and processing algorithms of the SMAP radiometer that outputs the first four raw moments of the receiver–system noise voltage in 16 frequency channels for measuring noise temperature and kurtosis, as well as cross-correlation products for measuring the third and fourth Stokes parameters. The ground-based processing algorithms utilize several detectors to identify RFI in the frequency, time, statistical, and polarization domains measured by the instrument. These detectors are then utilized to remove the contaminated time/bandwidth portions of the observation. Therefore, the Aquarius instrument and SMAP radiometer have the ability to flag RFI-affected samples, as well as mitigate the influence of RFI, and provide a measure of the level of RFI contamination.

Several surface-based and airborne L-band radiometers have been in operation for calibration and validation algorithm development activities during the pre- and post-launch periods for SMOS, Aquarius, and SMAP (Misra et al., 2013; Pardé et al., 2011; Delwart et al., 2008; Rautiainen et al., 2008). With this in mind, a hyperspectral L-band radiometer system was developed by Radiometrics Corporation©, Boulder, CO, and delivered to Environment and Climate Change Canada's (ECCC) Climate Research Division in 2010, that has the capability to detect broadband RFI and mitigate narrowband RFI over an expanded bandwidth with high frequency resolution, in a package that can be easily mounted on both tower and airborne platforms. This advanced dual polarization, hyperspectral L-band radiometer can be operated in the 385 channel hyperspectral mode which spans 1400 through $\approx$ 1550 MHz. The objectives of this paper are to provide an overview of the radiometer, characterize the performance and calibration, and describe a simple but effective method of separating out the thermal spectrum channels from those contaminated by narrowband RFI. Two evaluation datasets were utilized: ground-based measurements made through the 2014–2015 winter season in Saskatchewan, Canada, to monitor the freeze–thaw state of the surface soil layer and airborne measurements over sea ice acquired in the Canadian Arctic in April 2011.

2 Radiometer system

2.1 Radiometer architecture

During the initial design stage of the hyperspectral radiometer, it was known that RFI was commonly present in the protected band 1400–1427 MHz. Therefore, the radiometer was designed with a bandwidth expanded outside the protected band with the intention of improving the ability to detect adjacent RFI-free channels. The full radiometer bandwidth observes the 1375 to 1575 MHz spectrum in 512 channels ($\approx$ 391 kHz width) at both horizontal and vertical polarizations. The system described herein consists of a down-converter module, a digital processor module, and a conformal antenna with interconnect and power cables.

The radiometer down-converter/receiver serially measures antenna polarizations, a 50 ohm ambient load, and a calibrated noise diode that can be modulated with a CPU-controlled programmable attenuator. A bandpass filter follows the first antenna isolator to reduce intermodulation that might occur at the input of the first low noise amplifier (LNA). A synthesized local oscillator and selectable bandpass filters allow either a 25 MHz bandpass to be located within the 1375 to 1575 MHz receiver band or for the full 200 MHz to be sampled. The down-converted power is split

into two outputs with the first being a detected video output for operation as a Dicke radiometer. The second output is an intermediate frequency (IF) power output that is fed to a digital signal processor via a 400 megasamples/s 14 bit analog-to-digital (A2D) sampler for subsequent Cooley–Tukey type Fourier transformation. The Fourier transformation is accomplished in a Xilinx field programmable gate array (FPGA), which includes a blanking algorithm followed by the transform. The 1024 channels (512 horizontal and 512 vertical) are accumulated and passed over a PCI bus to a single board computer. The computer also controls the functions of the receiver.

The internal components of the receiver are mounted to a thick aluminum plate for stability and thermal uniformity. The plate is temperature controlled by Peltier junctions to within $\pm 0.03\,^{\circ}\mathrm{C}$ of $35\,^{\circ}\mathrm{C}$ and is in an enclosure separate from the digital signal processor. The system has a dynamic range of 70 dB. To reduce the effects of spectral leakage from adjacent bands of strong RFI, the channels near the edges of the 200 MHz receiver bandwidth are not used for analysis, and instead only 385 channels and ≈ 150 MHz bandwidth (1400 to 1550.5 MHz) are utilized. The 385 calibrated brightness temperature channels are each ≈ 391 kHz in width. The narrow bandwidth of the channels greatly enhances the ability to detect narrowband RFI intrusions compared to what would be realized if an intrusion fell in a broadband (e.g. 25 MHz) channel. The L-band radiometer system component and measurement specifications are listed in Table 1.

The antenna was designed to be compact ($51 \times 51 \times 6.5$ cm and ≈ 5 kg) for easy mounting on ground and airborne platforms. A shallow antenna depth was necessary for aircraft mounting to reduce drag, and so a 19-element air-loaded conformal muffin tin design was utilized (Fig. 1). The loss of this antenna and its combiners is less than 0.5 dB. The temperature of the antenna and of the two antenna-to-down converter cables are measured and recorded for system temperature and gain corrections. The antenna was designed with a 30° half-power beamwidth (−3 dB), with side lobes below −20 dB. The angle of incidence can be manually adjusted between measurements when in operation on the ground and is fixed at 40° when operated on an aircraft (SMAP viewing mode). At 40°, the large beamwidth of the radiometer antenna produces a footprint depth that approximates the height of the radiometer antenna above the surface, and a width that is approximately three-quarters the size of the depth.

The radiometer has six video states, which include observing the vertical antenna, vertical antenna plus noise diode, horizontal antenna, horizontal antenna plus noise diode, load, and load plus noise diode in one integration cycle. Each sample takes 0.5 ms; each time a state changes, the radiometer waits for 4 samples and then integrates for 22 samples. The radiometer observes all six states 50 times, with a ≈ 60 ms between each integration cycle to record system information, producing one scene measurement every ≈ 3.9 s for all channels and both polarizations. There can be some variance in the integration time due to the overhead associated with the thermal control and the settings of the synthesizer (0–1.5 s).

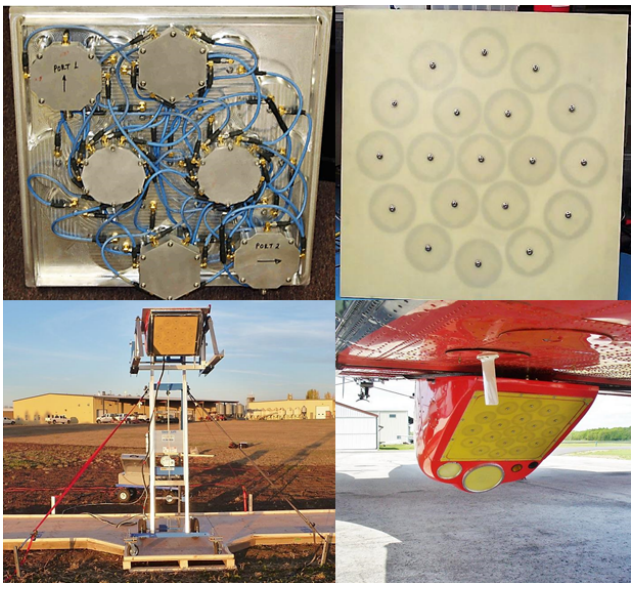

Figure 1. Conformal muffin tin antenna, back (top left) and front (top right), surface-based mobile platform (bottom left), and airborne platform (bottom right; aircraft fuselage mount includes deployment with higher frequency radiometers).

2.2 Radiometer calibration

A calibrated brightness temperature (T_B) is computed for each channel and polarization. The radiometer determines the T_B of the field of view (FOV) by measuring the receiver video voltage difference between the FOV (V_{sky}) and the internal load observations (V_{load}) and comparing this with the voltage difference realized by turning on the noise diode while at the internal load (V_{loadND}). This noise diode voltage enhancement is the measure of gain that determines the temperature difference between the internal load and V_{sky}.

$$V_{load} = g(T_{RCV} + T_{load} + \mathrm{Offset})^{\alpha} \quad (1)$$

$$V_{loadND} = g(T_{RCV} + T_{load} + \mathrm{Offset} + T_{ND})^{\alpha} \quad (2)$$

$$V_{sky} = g(T_{RCV} + T_{sky})^{\alpha} \quad (3)$$

The noise diode values (T_{ND}) are the gain reference for the radiometer and scale the voltage differences between the internal load measurements and the observations of the antenna. The offset values (Offset) calibrate the internal load temperature as seen by the radiometer receiver. T_{ND} and Offset are calculated using the following fixed calibration parameters: (α, $T_{ND}(0\,^{\circ}\mathrm{C})$, $T_{ND}\mathrm{TC}$, Offset(0 °C), and OffsetTC). However, due to the temperature dependence of gain and offset, these fixed values must first be temperature corrected using the case temperature in which the receiver is

Table 1. ECCC L-band radiometer component and measurement specifications.

Component	Specification
Radiometer receiver architecture	high sideband down conversion
Frequency range, GHz	1.40 to 1.55
Edge-to-edge IF bandpass, MHz	150 MHz (hyperspectral mode) or 25 MHz (broadband mode); user selectable
Hyperspectral mode	385 channels of $\approx$ 391 KHz width
Radiometric resolution, ΔT, kelvin	
Single observation, single channel	2.52
Single observation, 385 channels	0.13
Antenna HPBW, degrees	30
Side lobes, −dB	−20
Antenna type	conformal muffin tin antenna
Noise figure, dB	3.6
Receiver noise temperature, kelvin	374
Weight (antenna and receiver), kg	15
Voltage, vdc	18 to 32
Power, watts maximum	100
Dimensions: antenna housing	$60 \times 57 \times 42$ cm
Internal receiver temperature, Celsius	35 ($\pm$0.03)
Environmental: temperature	−50 to +50 °C
Measurement	**Specifications**
Nominal calibrated brightness temperature accuracy	$\approx$ 1.5 K
Integration cycle	$\approx$ 3.9 s
Warm-up time (typical)	20 min

housed, (T_{case} in °C), which fluctuates with the outside ambient operating temperature surrounding the receiver/antenna and all cables:

$$T_{\text{ND}} = T_{\text{ND}}(0\,^{\circ}\text{C}) + T_{\text{ND}}\text{TC} \cdot T_{\text{case}}, \tag{4}$$

$$\text{Offset} = \text{Offset}(0\,^{\circ}\text{C}) - \text{OffsetTC} \cdot T_{\text{case}}. \tag{5}$$

To determine the gain and offset values, measurements of at least two targets of known black body temperatures are required. The following equations are used to derive T_{B} from these measured data for each channel and each polarization (512 vertical channels (V-pol), 512 horizontal channels (H-pol)) from the observed scene. These equations take into account the internal temperatures of the receiver and the internal load, which are both set to 35 °C:

To calculate T_{B}, the gain (g) is calculated:

$$g = \left[\frac{V_{\text{loadND}}^{\frac{1}{\alpha}} - V_{\text{load}}^{\frac{1}{\alpha}}}{T_{\text{ND}}} \right]^{\alpha}. \tag{6}$$

The receiver temperature is then calculated:

$$T_{\text{RCV}} = \left(\frac{V_{\text{load}}}{g} \right)^{1/\alpha} + T_{\text{load}} - \text{Offset}. \tag{7}$$

Then T_{B} is

$$T_{\text{B}} = \left(\frac{V_{\text{sky}}}{g} \right)^{1/\alpha} - T_{\text{RCV}}. \tag{8}$$

The field calibration measurement techniques and post-processing procedures will be explained further in Sect. 3.2.

3 Methods

3.1 Sites and data collection

The L-band radiometer calibration accuracy and RFI mitigation approach was evaluated using ground-based measurements of brightness temperature over varying soil moisture and freeze–thaw conditions throughout the 2014–2015 winter season as part of an ECCC-led L-band freeze–thaw detection campaign. Continuous radiometer measurements were made from $\approx$ 2.75 m above the ground mounted on a moveable platform, at the University of Saskatchewan's Kernen Crop Research Farm within the city of Saskatoon (52.149° N; 106.545° W) (Roy et al., 2017). These temporally continuous measurements recorded in the same location were augmented with monthly visits to multiple sites with varying soil conditions and potentially changing RFI contributions across the Kenaston–Brightwater Creek soil monitoring network 85 km south of Saskatoon ($\approx$ 51.3° N, 106.5° W). Between 23 October 2014 and 24 April 2015, 16 three-target calibrations were measured between these two research sites (sky, ambient black body, and heated black body; see next section for descriptions of targets). During the campaign, regular radiometer stability-check measurements of each calibration

target, sky (91 measurements), ambient (19 measurements), and heated (13 measurements), were recorded. The calibration measurements were used to calibrate the radiometer, while the stability-check measurements were used to check that the instrument was stable and provided an independent measure of whether the current calibrations were still valid.

The L-band radiometer was also deployed in the Canadian Arctic during the Polar Airborne Measurements and Arctic Regional Climate Model Simulation Project (PAMARCMIP) in 2011. During the campaign, the L-band radiometer was mounted aft-viewing (along-track), on the Alfred Wegener Institute's Polar 5 research aircraft, with a 40° incidence angle. During one of the research flights, the aircraft flew at an altitude of ≈ 100 m over first-year sea ice in Nares Strait (78.797° N, 74.059° W), which would normally produce an approximate radiometer footprint of $\approx 96\,\text{m} \times \approx 74\,\text{m}$ if the radiometer antenna were stationary. However, the aircraft platform was travelling at an average ground speed of $\approx 65\,\text{m}\,\text{s}^{-1}$; with the radiometer's approximate 4 s integration cycle, the average footprint size was ≈ 74 m wide (across-track) and ≈ 356 m in the along-track direction of travel.

Both the L-band soil and sea ice measurements were utilized to assess the effectiveness of the RFI removal algorithm. Both constant and intermittent continuous wave narrowband RFI was observed during all flights and calibrations during the PAMARCMIP 2011 campaign. Some similarities in detected patterns of RFI were noted between the PAMARCMIP 2011 campaign and other research campaigns. It was suspected that at least some of the RFI detected by the hyperspectral L-band radiometer emanates from the radiometer system itself. To investigate, the radiometer system was placed in a closed metal shipping container, acting like a Faraday cage, and different components of the system (generator, power supply, digital signal processing computer) were removed from the container one-by-one to investigate the change in measured T_B. It was noted that both the digital signal processing computer and the radiometer receiver were sources of intermittent narrowband L-band RFI. Mitigation of these RFI sources involved housing the computer in an enclosed metal box, while the position of the radiometer receiver was mounted behind the antenna. These changes reduced the intensity and frequency of occurrence of RFI detected, but it did not completely remove their intermittent contribution. However, due to the hyperspectral nature of this L-band radiometer, the intermittent narrowband RFI can be further mitigated through post-processing of the data.

3.2 Calibration measurement procedure/post-processing

The absolute accuracy of a radiometer is dependent on the internal calibration procedure, the uncertainty of the external calibration, and the inherent stability of the radiometer's internal electronics. An external calibration is necessary to account for losses and reflections in components of the radiometer system outside of the receiver and to account for changing environmental variables. Surface-based and airborne radiometer systems are exposed to a stressful and ever-changing environment: the system is typically not mounted permanently but is assembled and disassembled for each campaign; the power is turned on and off repeatedly each day and environmental temperature can vary significantly between measurements.

During aircraft campaigns there is a risk that strong RFI may be present at airports due to airport radars and air route surveillance (Hallikainen et al., 2010; Skou et al., 2010; Le Vine, 2002), which may pose a challenge when trying to calibrate at these locations. Therefore, a field-transportable two-temperature calibration target was built to couple with the ECCC radiometer antenna. The calibration system was built into a $70 \times 70 \times 70$ cm shipping container that splits in half, with one side heated and the other side an ambient black body target. A fan circulates air through the open cell black body foam in which five precision temperature sensors are embedded. The heated "warm" side is controlled at ≈ 343 K, while the "cold" side is controlled by the outside ambient temperature. A three-point calibration procedure using the sky, ambient, and heated warm targets was developed to account for the radiometer's calibration nonlinearity and improve the accuracy over the full range of measured T_B. The reference sky T_B at L-band was considered to be ≈ 5 K for both polarizations based on previously published data from both measured and modelled sources (Pellarin et al., 2016; Lemmetyinen et al., 2016; Le Vine et al., 2005; Delahaye et al., 2002).

We utilize the ground-based calibration measurements from Saskatchewan to illustrate the calibration procedure. The post-processing of the calibration measurements involves the optimization of calibration coefficients, which takes place in two steps. First, all five calibration coefficients (α, $T_\text{ND}(0\,^\circ\text{C})$, $T_\text{ND}\text{TC}$, Offset(0 °C), and OffsetTC) are optimized for all 385 channels and both polarizations, using all 16 three-target calibration measurements acquired between October 2014 and April 2015. This first step was done to take into account the changes in the environmental operating temperature (T_case) of the radiometer between calibration dates. Measured T_case from all 16 three-target calibrations ranged from -18.1 to 23.5 °C for the entire campaign. To assess the sensitivity of the radiometer to variations in T_case, calibrated T_Bs were calculated for the 9 November ambient calibration measurements, computed using the exact same set of coefficients, with the exception of the T_case value. The minimum and maximum observed T_case values were used as inputs (-18.1 and 23.5 °C), leading to a difference of ≈ 10 K (269.4 K vs. 259.3 K) in the calculated T_B of the ambient calibration target, highlighting the importance of applying a temperature correction to reflect changes in the environmental operating temperatures of the radiometers. After optimizing the coefficients with T_case, a robust local regression using

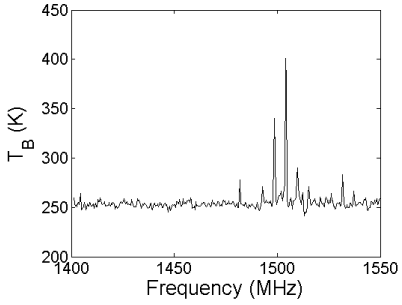

Figure 2. Horizontally polarized T_B spectrum of the ambient black body target (measured physical temperature of 251 K) during a stability-check measurement. Narrowband RFI peaks are observed around 1500 MHz. (11 February 2015 20:17 UTC).

weighted linear least squares and a second-degree polynomial model was applied to create a smooth calibration curve for each coefficient for all channels. Applying the second-degree polynomial model to the calibration coefficients removes some of the inter-channel variability, but it can also be used to apply meaningful coefficients to RFI-affected channels. If a narrow group of channels is contaminated with intermittent RFI during the calibration procedure (Fig. 2), the smoothed polynomial calibration curve can apply adjacent calibration coefficients to the RFI-affected channels so that usable data can still be acquired at these frequencies.

The results from completing step 1 of the post-processing are used to fix the coefficients for OffsetTC, T_{ND}TC, and α as constants. Secondly, the optimization results for the coefficients $T_{ND}(0\,°C)$ and Offset(0 °C) from the first post-processing step are used as a first guess to run the inversion model again, this time to produce a set of new calibration coefficients for $T_{ND}(0\,°C)$ and Offset(0 °C) for each date of the 16 three-target calibrations to correct for inherent instability of the radiometer's internal electronic components over the course of the campaign. The optimized values for $T_{ND}(0\,°C)$ and Offset(0 °C) are then interpolated in time between calibration measurements with simple linear regression. These interpolated calibration coefficients are then used to calculate the final "science-ready" T_B for all measurements recorded between the calibration dates and were also applied to all radiometer calibration stability-check measurements to assess the calibration accuracy for the campaign.

3.3 Hyperspectral RFI mitigation approach

A number of L-band RFI identification and mitigation methods have previously been proposed and developed into hardware for both airborne and satellite systems (Guner et al., 2007; Forte et al., 2011; Pardé et al., 2011; Misra et al., 2009), but the hyperspectral system described in this paper has the capability of identifying RFI-free channels over an expanded 1400–1550 MHz spectrum. The advantage of observing over a larger bandwidth increases the likelihood of observing RFI-free channels but also results in the recording of more frequent (legal) RFI occurrences outside the protected band. However, this higher frequency of observed RFI outside the protected band does not affect the performance of the RFI mitigation approach described herein, as long as the percent of contaminated bandwidth does not become exceedingly large (see Sect. 4.2). This hyperspectral radiometer system assumes that the natural T_B of a scene is a Gaussian distribution and that the thermal spectra from the observed scene are a near constant T_B across the 1400–1550 MHz bandpass, with minimal observed variability due to the receiver's noise equivalent temperature difference (ΔT), calibration error, and some small variance from within the scene (see Table 1). A simple but effective method of separating out the thermal signal plus the receiver noise and calibration uncertainty from RFI-contaminated channels is to sort the observed T_B spectra in ascending order. The thermal channels sort to the low values, with the spectra gradually increasing by several kelvin due to the receiver noise, calibration errors, and variability within the scene. The RFI-contaminated channels are then identified where the brightness begins to rise out of the expected thermal spectrum. However, it is challenging to identify the exact point at which the RFI begins this rise out of the expected thermal spectrum because of the unknown nature and source of the RFI contamination. This dilemma led the authors to develop an RFI mitigation approach that identifies a representative RFI-free T_B value for this spectrum, using a third-order polynomial of the sorted T_B spectra in ascending order. The second derivative of the slope of this cubic polynomial is derived. For a clean thermal spectrum with random noise, the mean value is a close approximation of the T_B at the inflection point where the second derivative goes from negative to positive. For a spectrum contaminated with RFI, the mean value of the spectrum is skewed higher by the RFI-affected channels; however, the T_B at the inflection point where the second derivative of the third-order polynomial of sort-rank vs. T_B goes from negative to positive is still representative of the mean value of the same scene without RFI (within ≈ 2 K for a spectrum contamination of up to ≈ 9 %; see Sect. 4.2), and therefore the T_B value at the inflection is used for subsequent analysis and is considered the RFI mitigated result. Figure 3 illustrates the horizontal polarized T_Bs of one integration cycle of the ambient calibration target (251 K) shown in Fig. 2, which is a sum of the natural thermal signal (Gaussian) and RFI (not Gaussian). The data are sorted into ascending order represented by the blue-dashed line. The red dot in Fig. 3 is the inflection point (251.9 K), representative of the mean T_B of the same scene without RFI. The mean value of the full spectrum in Fig. 3 (RFI included) is 255.2 K. To the right of the inflection point are the natural thermal spectrum values larger than the mean T_B value (the high side of the Gaussian distribution of thermal energies) and the RFI-affected channels. To the left are the values of the natural thermal spectrum smaller than the mean value, but only the T_B value at the inflection point

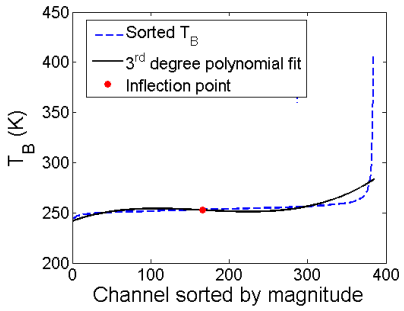

Figure 3. Horizontally polarized T_B of one integration cycle of the ambient calibration target (251 K; same spectrum as Fig. 2) sorted into ascending order. A third-order polynomial (black line) is used to approximate the curve of the sorted T_B with the mean T_B of the Gaussian distribution identified as occurring at the inflection point where the second derivative of this curve goes from negative to positive (red dot).

is used to define the observed T_B of the scene. The inflection point T_B become less representative of the scene as the spectrum being analyzed becomes exceedingly non-normal due to overwhelming RFI contamination, which results in unrealistic T_B values that are relatively easy to detect using a visual inspection of the spectrum and/or of the time series data plots. The spectrum can also become non-normal from limiting the application of the RFI mitigation approach to a narrow bandwidth, with too few channels creating a uniform, short-tailed distribution when the scene is RFI-free. In instances where a narrow bandwidth is employed and the scene is RFI-free, the midpoint of the spectrum is chosen to represent the mean of the scene rather than the inflection point. This RFI mitigation approach is applied to each polarization separately, typically for all 385 channels in the 1400–1550 MHz spectrum. All subsequent temporal averaging of the T_B measurements is then applied to the RFI-mitigated data.

3.4 Sensitivity analysis of the RFI mitigation approach using modelled data

To evaluate and validate the RFI mitigation approach, a Monte Carlo experiment was conducted to create synthetic L-band spectra (O'Haver, 2016), with random RFI peaks. The experiment tested two main characteristics of RFI that can affect the performance of the RFI mitigation algorithm: (1) the number of peaks within the spectrum (no. peaks) and (2) the bandwidth of those peaks (ω), represented by the number of channels ($1\omega = 390.625$ kHz). For each different combination of no. peaks (0–20) and ω (1–3–5–10 channels), 1000 replicate simulations were run and the RFI removal algorithm was applied to the synthetic spectra. The mean T_B of the synthetic scene was set to 250 K with a random noise of 3.6 K added to all channels, representing the typical standard deviation measured by the radiometer from an unfiltered RFI-free single integration cycle measured across the 1400–1550 MHz spectrum. The peak amplitudes were randomly set based on absolute values of a normal distribution with mean 0 and standard deviation 100. For all 1000 replicates of the different combinations of no. peaks and ω, a mean T_B value (T_{B-mean}) of the RFI mitigation results and a standard deviation were calculated. The performance of the RFI mitigation approach was assessed by comparing the difference between the mean RFI mitigation results to the 250 K mean T_B of the synthetic spectrum. If the RFI mitigation results were within 2 K of the set 250 K mean of the synthetic spectrum, then the RFI mitigation approach was considered successful. A 2 K threshold was chosen because it is slightly larger than the combination of the calibration accuracy (≈ 1.5 K; see Sect. 4.1) and the radiometer's radiometric resolution for the entire 150 MHz spectrum (0.13 K; see Table 1) added together.

4 Results

In this section, we present the results of the calibration accuracy assessment and radiometer stability observed during the 2014–2015 Saskatchewan soil freeze–thaw detection campaign. A sensitivity analysis using modelled data to assess the performance of the hyperspectral RFI mitigation technique under varying degrees of RFI saturation using a Monte Carlo approach is provided. The sensitivity analysis is followed by two examples of the hyperspectral RFI mitigation technique applied to L-band surface-based radiometer measurements of unfrozen bare soil in Saskatchewan and of first-year sea ice from airborne observations in the Canadian Arctic.

4.1 Radiometer calibration results and instrument stability evaluation

The calibration accuracy and radiometer instrument stability were examined using the surface-based radiometer measurements recorded in Saskatchewan from October 2014 to April 2015. Figure 4 shows the optimization results of the first step of the calibration post-processing, where all calibration coefficients ($T_{ND}(0\,°C)$, Offset(0 °C), T_{ND}TC, OffsetTC, and α) are optimized for T_{case} at the same time using all 16 three-target calibrations. The variability in the optimized coefficient results (dashed-green line in Fig. 4) is likely a direct result of the varying amounts of RFI present during each calibration date, emitted by both external sources and internal system components. RFI intrusions can be polarization specific, as illustrated by the differences in the dashed-green line between the H-pol and V-pol plots. This RFI-induced noise in the optimization results is smoothed using a robust local regression using weighted linear least squares and a second-degree polynomial model (solid blue line in Fig. 4).

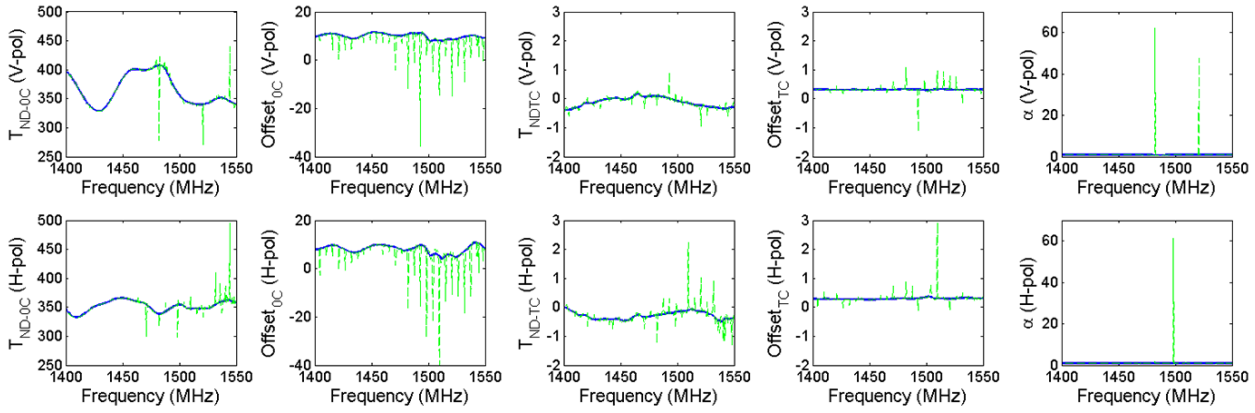

Figure 4. Optimization results for the following calibration coefficients plotted from left to right: $T_{ND}(0\,°C)$, Offset(0 °C), T_{ND}TC, OffsetTC, and α for V-pol (top) and H-pol (bottom) for all frequencies. Green line: optimization results of all 16 calibrations; blue line: robust local regression using weighted linear least squares and a second-degree polynomial model.

Using the results of the smoothed (blue line in Fig. 4) calibration coefficients, α, T_{ND}TC, and OffsetTC are held constant, while the smoothed results for the coefficients $T_{ND}(0\,°C)$ and Offset(0 °C) are used as a first guess, to run the inversion model again. A set of new calibration coefficients for $T_{ND}(0\,°C)$ and Offset(0 °C) for each date of the 16 three-target calibrations is produced. These coefficients are used to correct for sensor drift of the radiometer over the course of the campaign (Fig. 5: red dots – for the 1451 MHz channel). The $T_{ND}(0\,°C)$ optimization results in Fig. 5 identify some random sensor drift at the beginning of the season with a large step change shift observed between the 14 and 31 January calibrations. This step change was possibly related to a power supply failure that occurred on 18 January (replaced on 21 January). The $T_{ND}(0\,°C)$ calibration coefficients then trended upward, stabilizing near the end of March. The Offset(0 °C) optimization results in Fig. 5 identify a more random pattern throughout the campaign, with the exception of a noticeable drop in Offset(0 °C) value in February, which remains unexplained.

To account for radiometer drift between external calibrations, $T_{ND}(0\,°C)$ and Offset(0 °C) were interpolated in time with simple linear regression, and these interpolated coefficients were then used to calculate daily calibrated T_B (Fig. 5: black lines). In most instances, the interpolated coefficients are representative of the gradual radiometer sensor drift due to the inherent instabilities of the internal electronics. However, there are exceptions, such as when the radiometer sensor undergoes a step change in stability, as took place between 14 and 31 January 2015. The change in calculated coefficients between the 14th and 31st calibration dates was several times larger than the difference in coefficients between all other dates, and thus the application of a simple linear regression to interpolate the coefficients in time between these dates may not be the best course of action because applying the interpolated coefficients implies a continuous drift

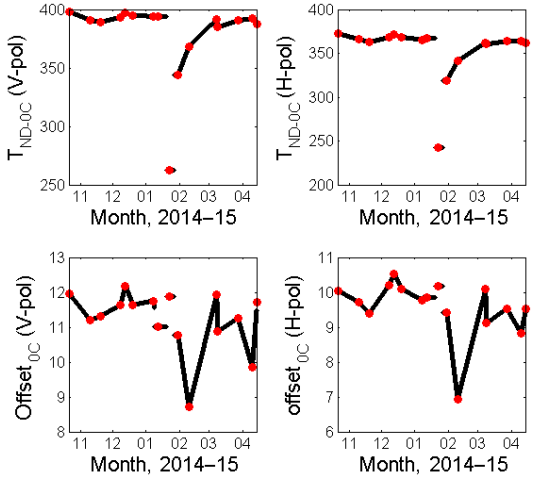

Figure 5. Example of the V-pol (left) and H-pol (right) inverted calibration coefficient $T_{ND}(0\,°C)$ and Offset(0 °C) for the 1451 MHz channel during the 16 three-target calibration measurements (red dots) conducted between October 2014 and April 2015. The black line is the interpolation of calibration coefficient between measurement dates (red dots).

in coefficients instead of the observed step-wise change in system stability. Therefore, all data that fell between these two calibration dates made use of the non-interpolated coefficients from the calibration date that was closest. This time series of calibration coefficients highlights the importance of regularly verifying the calibration of an instrument during a research campaign.

To evaluate the radiometer's calibration accuracy, the interpolated calibration coefficients were used to produce calibrated T_B for measurements acquired during all radiometer stability-checks of the sky (T_{Bsky}), ambient black body targets, and heated warm black body targets made at the Kernen Crop Research Farm and the Kenaston–Brightwater Creek

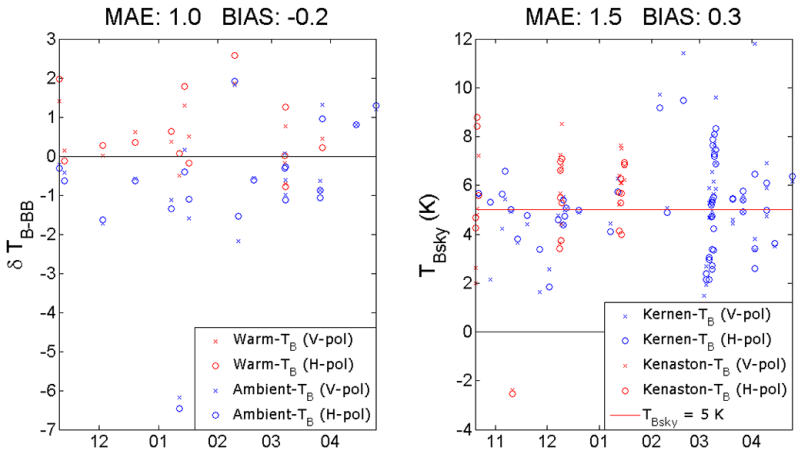

Figure 6. The left plot illustrates the difference between measured black body physical temperature (BB) and the L-band radiometer measurement (δT_B). The right plot illustrates the difference between the theoretical T_{Bsky} and the L-band radiometer measurements from the stability-check measurements. The x axis is in time (month of the year).

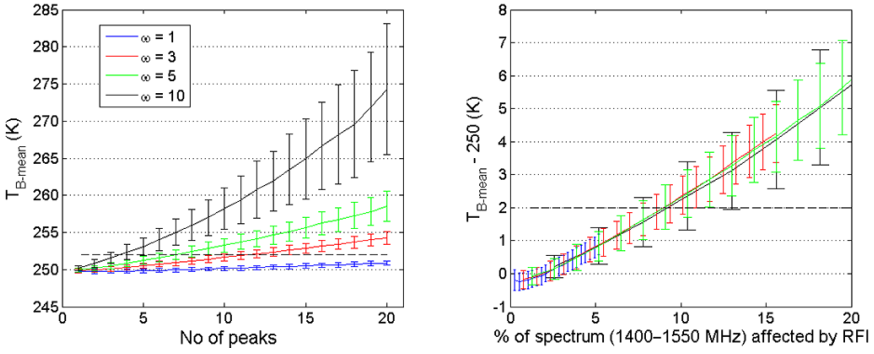

Figure 7. For all 1000 replicates of the different combinations of peaks (0 up to 20) and bandwidths (1–3–5–10), a mean T_B and associated standard deviation (error bars) are plotted (solid lines) for comparison to the mean T_B of the synthetic spectra (set to 250 K). A horizontal dashed line has been added to both plots, highlighting the RFI mitigation results within 2 K of the synthetic spectra mean.

soil monitoring network in Saskatchewan between October 2014 and April 2015. These stability-check measurements were independent of those used to produce the calibration coefficients. The difference between the black body physical temperature and radiometer T_B are calculated (δT_{B-BB}). Mean absolute error (MAE) of 1 K (Fig. 6 left) with ambient and warm targets and 1.5 K (Fig. 6 right) with sky measurements from both the Kernen and Kenaston sites ($T_{Bsky} \approx 5$ K from Lemmetyinen et al., 2016; Pellarin et al., 2016; Le Vine et al., 2005). The biases are lower than 0.3 K. For black body targets, only one point gives errors higher than 3 K. This single occurrence is likely associated with an error in recording the black body physical temperature during the stability-check. The higher error in the sky measurements could be related to the fact that the sky emission might vary slightly depending upon the observed portion of the sky due to the variability in sky background temperatures measured when the antenna beamwidth crosses the galactic plane (increases by 1–3 K) and due to potential contributions from the sun and moon (Delahaye et al., 2002; Le Vine et al., 2005). Further analysis of these effects will be evaluated in future campaigns. The response to soil freeze–thaw state and soil moisture fluctuations is on the order of 30 to 50 K, so a measurement time series with an MAE of less than 1.5 K and minimal bias can be considered very robust for these applications.

4.2 Sensitivity analysis of the RFI mitigation approach using modelled data

The performance of the RFI mitigation approach was assessed by comparing the difference between the mean RFI mitigation results to the set 250 K mean T_B of the synthetic spectra. If the RFI mitigation results were within 2 K of the mean 250 K of the synthetic spectrum, then the RFI mitigation approach was considered successful (see Sect. 3.4 for assessment criteria). Figure 7 (left) illustrates that for narrow RFI peaks ($\omega = 1$) the RFI mitigation approach can retrieve the mean T_B from the scene to within 2 K independent of

Table 2. The RFI mitigation approach was applied to these synthetic spectra to determine the maximum number of RFI peaks and total bandwidth/proportion of the spectrum that can be contaminated with RFI while still returning a result within 2 K of the mean.

Number of channels/ bandwidth (MHz)	Maximum number of peaks	Total bandwidth (MHz) of RFI-affected channels	Proportion of ≈ 150 MHz spectrum
1 (≈ 0.39 MHz)	20	7.8	5.2 %
3 (≈ 1.17 MHz)	11	12.9	8.6 %
5 (≈ 1.95 MHz)	6	11.7	7.8%
10 (≈ 3.91 MHz)	3	11.7	7.8%

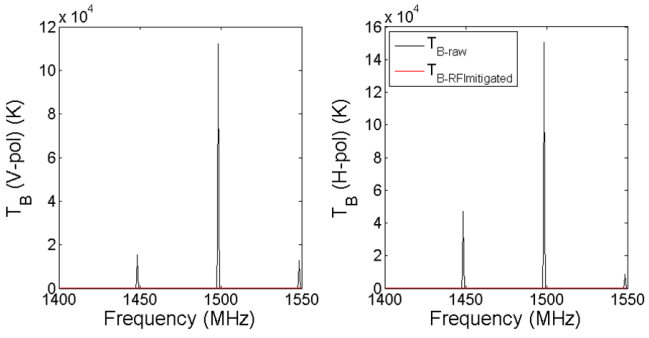

Figure 8. V-pol (left) and H-pol (right) T_B measured at Kernen crop research farm during data logger RFI emission (25 October 2014 03:00:00 UTC).

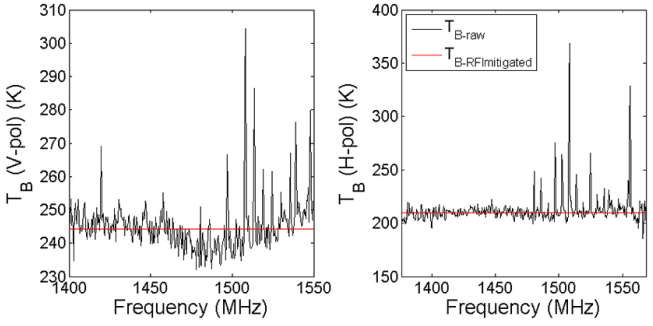

Figure 9. V-pol (left) and H-pol (right) T_B measured at Kernen crop research farm without data logger RFI emission (25 October 2014 03:00:30 UTC). The red line is representative of the RFI-mitigated T_B results.

the number of peaks (up to a maximum of 20 in this experiment). However, as both the bandwidth of the RFI peaks gets larger, and the number of peaks of larger bandwidth RFI sources increases, the performance of the RFI mitigation algorithm declines. Figure 7 (right) plots the decline in algorithm performance as a function of percent of spectrum (1400–1550 MHz) contaminated by RFI. Table 2 illustrates the results of the Monte Carlo experiment, indicating the proportion of total spectrum that can be contaminated with RFI intrusions, while still being able to determine the mean T_B value within 2 K of the 250 K synthetic spectra mean. The RFI mitigation approach was successful at retrieving an accurate mean T_B with up to ≈ 9 % of the spectrum contaminated with RFI.

4.3 Application of the RFI mitigation approach using experimental data

During the Saskatchewan L-band soil campaign in 2014–2015, continuous surface-based measurements looking at a bare soil surface at 40° incidence angle were recorded. Stevens HydraProbe soil moisture and temperature probes were installed within the FOV of the radiometer and were recorded using a CR1000 data logger. The logger recorded data at 30 min intervals, coinciding with intense repeated, short duration, narrowband RFI emission at ≈ 1450 MHz (V-pol = 1760 K; H-pol = 5530 K) and ≈ 1550 (V-pol = 11 218 K; H-pol = 31 044 K), as illustrated in Fig. 8. These high T_B peaks likely emitting from the logger show a significant contrast with normal continuous measurements where occasional relatively low RFI narrow peaks are seen (Fig. 9). This example allows for a comparison of the spectra over the same ground conditions with a significant RFI intrusion (Fig. 8) compared to one with nominal "background" RFI present (Fig. 9).

For both cases, the mean 1400–1550 MHz spectrum T_B was calculated with and without the RFI intrusion and compared with the RFI mitigation algorithm described in this paper with the results provided in Table 3. When the hyperspectral radiometer's RFI mitigation approach is applied to an observation affected by a powerful narrowband RFI source, it is able to return a mean T_B value within < 2 K of the same scene when only nominal background RFI is present. A broadband radiometer would have likely measured an average T_B of 1761.3 K (H-pol) and 955.6 K (V-pol) while observing an RFI emission with this level of intensity over the same spectrum. This example with experimental data demonstrates the capability of the radiometer and RFI mitigation approach for determining a representative RFI-free T_B value even in the presence of strong, narrowband RFI intrusions.

The mean spectrum T_B and the results from our RFI mitigation technique were also compared for airborne observations over first-year sea ice, which contained both narrowband (H-pol) and broadband (V-pol) RFI (Fig. 10). The difference between the 1400–1550 MHz spectrum average T_B

Table 3. Mean T_B with and without RFI mitigation at the Kernen crop research farm for measurements of unfrozen bare soil at 40° with and without data logger RFI emission (25 October 2014 03:00:30 UTC).

	No RFI mitigation	RFI mitigation
T_B (H-pol) without data logger emission	212.2	210.0
T_B (V-pol) without data logger emission	245.8	244.2
T_B (H-pol) with data logger emission	1761.3	210.9
T_B (V-pol) with data logger emission	955.6	246.0

Table 4. Mean T_B with and without RFI mitigation from airborne measurements over first-year sea ice in Nares Strait, Canadian Arctic (23 April 2011 16:25 UTC).

	No RFI mitigation	RFI mitigation
T_B (H-pol)	247.3	244.3
T_B (V-pol)	261.3	255.8

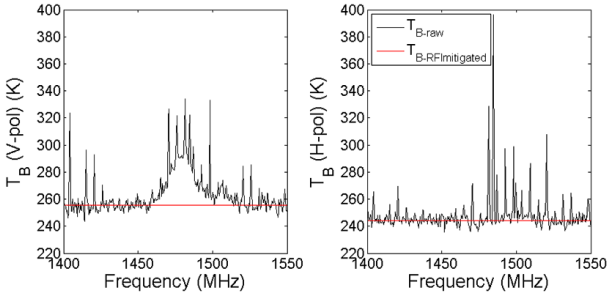

Figure 10. V-pol (left) and H-pol (right) T_B measured over first-year sea ice in Nares Strait, Canadian Arctic (23 April 2011 16:25 UTC). Note the V-pol broadband RFI intrusion. The red line is representative of the RFI-mitigated T_B results.

and the RFI mitigation inflection point T_B is shown in Table 4, with a T_B difference of 5.5 K at V-pol and 3.0 K at H-pol, highlighting that some RFI may add only a few kelvin to the observed scene and may be harder to detect utilizing a traditional broadband radiometer.

5 Conclusions

This paper describes a 385-channel hyperspectral L-band radiometer system. Using a three-point calibration procedure, mean absolute errors of 1 K for ambient and warm targets and 1.5 K for a cold sky reference were determined. Because of the hyperspectral measurements, both narrowband and broadband RFI intrusions can be detected. A simple and straightforward RFI mitigation approach is effective in separating out powerful narrowband RFI-affected frequencies to within 2 K of the natural thermal emission when the RFI is from narrowband sources, contaminating up to $\approx 9\,\%$ of the observed spectrum. The performance of the RFI mitigation approach declines with the presence of increasing bandwidth (broadband) sources of RFI; however, the system still has the means to quantify the strength and type of interference with its compact design for mounting on both surface and airborne platforms, making this an ideal tool for calibration and validation activities of spaceborne L-band sensors. The examples of RFI intrusions during previous research campaigns also highlight the potentially high level of RFI exposure facing broadband L-band radiometers in any environment due to both powerful illegal ground transmissions and subtle unintentional spurious emissions from complimentary research equipment.

6 Data availability

The data will be made available at http://donnees.ec.gc.ca/data/ archived under the same title as the published paper: "Radio-frequency interference mitigating hyperspectral L-band radiometer". For further information please contact the corresponding authors.

Acknowledgements. The authors would like to recognize the important contributions of Mike Harwood, Ka Sung, and Mark Couture in their efforts towards the successful installation, programming, and processing of the airborne data. Thanks to Lauren Arnold, Arvids Silis, and Bruce Cole for running the surface-based radiometer system for an entire winter season in Saskatchewan. Thanks to staff at Radiometrics Inc. and Walter Strapp for all their work on the design, construction, and testing of the hyperspectral L-band radiometer. Thanks to the Canadian Space Agency and NSERC for financial support to the authors, allowing for further development of the hyperspectral L-band data processing procedures.

Edited by: M. Zribi
Reviewed by: two anonymous referees

References

Anterrieu, E. and Khazâal, A.: One year of RFI detection and quantification with L1a signals provided by SMOS reference radiometers, Int. Geosci. Remote Sens., 2245–2248, 2011.

Aksoy, M. and Johnson, J. T.: A study of SMOS RFI over North America, Int. Geosci. Remote Sens., 10, 515–519, 2013.

Delwart, S. Bouzinac, C., Wursteisen, P., Berger, M., Drinkwater, M., Martin-Neira, M., and Kerr, Y.: SMOS Validation and the COSMOS campaigns, Int. Geosci. Remote Sens., 46, 695–704, 2008.

Delahaye, J.-Y., Golé, P., and Waldteufel, P.: Calibration error of L-band sky-looking ground-based radiometers, Radio Sci., 37, 11-1–11-11, 2002.

Entekhabi, D., Yueh, S., O'Neill, P. E., Wood, E. F., Njoku, E. G., Entin, J. K., and Kellogg, K. H.: The NASA Soil Moisture Active Passive (SMAP) Mission Status and Early Results, Geophys. Res. Abstr., EGU2015-5973, EGU General Assembly 2015, Vienna, Austria, 2015.

Fanise, P., Pardé, M., Zribi, M., Dechambre, M., and Caudoux, C.: Analysis of RFI identification and mitigation in CAROLS radiometer data using a hardware spectrum analyser, Sensors, 11, 3037–3050. 2011.

Forte, G. F., Tarongi, J. M., and Camps, A.: Hardware implementation of a wavelet-based radio frequency interference mitigation algorithm for microwave radiometers, Int. Geosci. Remote Sens., 2241–2244, 2011.

Hallikainen, M., Kainulainen, J., Seppanen, J., Hakkarainen, A., and Rautiainen, K.: Studies of radio frequency interference at L-band using an airborne 2-D interferometric radiometer, Int. Geosci. Remote Sen., 2490–2491, 2010.

Guner, B., Johnson, J. T., and Niamsuwan, N.: Time and frequency blanking for radio-frequency interference mitigation in microwave radiometry, IEEE T. Geosci. Remote, 45, 3672–3679, 2007.

ITU: No. 5.340 of Radio Regulations (RR) of the International Telecommunications Union – Radiocommunications sector (ITU-R), Article 5, Radio Regulations, Vol. 1, Edition of 2012, available at: https://www.itu.int/pub/R-REG-RR-2012 (last access: 11 October 2016), 2012.

Kaleschke, L., Tian-Kunze, X., Maaß, N., Mäkynen, M., and Drusch, M.: Sea ice thickness retrieval from SMOS brightness temperatures during the Arctic freeze-up period, Geophys. Res. Lett., 39, L05501, doi:10.1029/2012GL050916, 2012.

Kaleschke, L., Tian-Kunze, X., Maaß, N., Beitsch, A., Wernecke, A., Miernecki, M., Müller, G., Fock, B. H., Gierisch, A. M., Schlünzen, K. H., and Pohlmann, T.: SMOS sea ice product: Operational application and validation in the Barents Sea marginal ice zone, Remote Sens. Environ., 180, 264–273, 2016.

Kerr, Y. H., Waldteufel, P., Wigneron, J. P., Delwart, S., Cabot, F. O., Boutin, J., Escorihuela, M. J., Font, J., Reul, N., Gruhier, C., and Juglea, S. E.: The SMOS mission: New tool for monitoring key elements of the global water cycle, IEEE Proc., 98, 666–687, 2010.

Khazâal, A., Cabot, F., Anterrieu, E., and Soldo, Y.: A kurtosis-based approach to detect RFI in SMOS image reconstruction data processor, IEEE T. Geosci. Remote Sens., 52, 7038–7047, 2014.

Lagerloef, G., de Charon, A., and Lindstrom, E.: Ocean salinity and the Aquarius/SAC-D mission: A new frontier in ocean remote sensing, Mar. Technol. Soc. J., 47, 26–30, 2013.

Lemmetyinen, J., Schwank, M., Rautiainen, K., Parkkinen, T., Mätzler, C., Wiesmann, A., Wegmüller, U., Derksen, C., Toose, P., Roy, A., and Pulliainen, J.: Snow density and ground permittivity retrieved from L-Band radiometry: application to experimental data, Remote Sens. Environ., 180, 377–391, 2016.

Le Vine, D. M.: ESTAR experience with RFI at L-band and implications for future passive microwave remote sensing from space, Int. Geosci. Remote Sens., 2, 847–849, 2002.

Le Vine, D. M., Abraham, S., Kerr, Y., Wilson, W. J., and Skou, N.: Comparison of Model Prediction With Measurements of Galactic Background Noise at L-Band, IEEE T. Geosci. Remote, 43, 2018–2023, 2005.

Le Vine, D. M., de Matthaeis, P., Ruf, C. S., and Chen, D. D.: Aquarius RFI detection and mitigation algorithm: Assessment and examples, IEEE T. Geosci. Remote, 52, 4574–4584, 2014.

Misra, S., Mohammed, P. N., Güner, B., Ruf, C. S., Piepmeier, J. R., and Johnson, J. T.: Microwave radiometer radio-frequency interference detection algorithms: A comparative study, IEEE T. Geosci. Remote, 47, 3742–3754, 2009.

Misra, S., Johnson, J., Aksoy, M., Peng, J., Bradley, D., O'Dwyer, I., Padmanabhan, S., Dawson, D., Chazanoff, S., Latham, B., and Gaier, T.: SMAP RFI mitigation algorithm performance characterization using airborne high-rate direct-sampled SMAPVEX 2012 data, Int. Geosci. Remote Sens., 41–44, 2013.

O'Haver, T.: Software for peak finding and measurement, in: A Pragmatic Introduction to Signal Processing with application in scientific measurement, 1–142, available at: https://terpconnect.umd.edu/~toh/spectrum/IntroToSignalProcessing.pdf (last access: 3 November 2016), 2016.

Oliva, R., Daganzo, E., Richaume, P., Kerr, Y., Cabot, F., Soldo, Y., Anterrieu, E., Reul, N., Gutierrez, A., Barbosa, J., and Lopes, G.: Status of Radio Frequency Interference (RFI) in the 1400–1427 MHz passive band based on six years of SMOS mission, Remote Sens. Environ., 180, 64–75, 2016

Pardé, M., Zribi, M., Fanise, P., and Dechambre, M.: Analysis of RFI issue using the CAROLS L-band experiment, IEEE T. Geosci. Remote, 49, 1063–1070, 2011.

Pellarin, T., Mialon, A., Biron, R., Coulaud, C., Gibon, F., Ferr, Y., Lafaysse, M., Mercier, B., Morin, S., Redor, I., Schwank, M., and Völksch, I.: Three years of L-band brightness temperature measurements in a mountainous area: Topography, vegetation and snowmelt issues, Remote Sens. Environ., 180, 85–98, 2016.

Piepmeier, J. R., Johnson, J. T., Mohammed, P. N., Bradley, D., Ruf, C., Aksoy, M., Garcia, R., Hudson, D., Miles, L., and Wong, M.: Radio-frequency interference mitigation for the soil moisture active passive microwave radiometer, IEEE T. Geosci. Remote, 52, 761–775, 2014.

Rautiainen, K., Kainulainen, J., Auer, T., Pihlflyckt, J., Kettunen, J., and Hallikainen, M. T.: Helsinki University of Technology L-band airborne synthetic aperture radiometer, IEEE T. Geosci. Remote, 46, 717–726, 2008.

Rautiainen, K., Lemmetyinen, J., Schwank, M., Kontu, A., Ménard, C. B., Mätzler, C., Drusch, M., Wiesmann, A., Ikonen, J., and Pulliainen, J.: Detection of soil freezing from L-band passive microwave observations, Remote Sens. Environ., 147, 206–218, 2014.

Rautiainen, K., Parkkinen, T., Lemmetyinen, J., Schwank, M., Wiesmann, A., Ikonen, J., Derksen, C., Davydov, S., Davydova, A., Boike, J., and Langer, M.: SMOS prototype algorithm for detecting autumn soil freezing, Remote Sens. Environ., 180, 346–360, 2016.

Roy, A., Royer, A., Derksen, C., Brucker, L., Langlois, A., Mialon, A., and Kerr, Y. H.: Evaluation of Spaceborne L-Band Ra-

diometer Measurements for Terrestrial Freeze/Thaw Retrievals in Canada, IEEE J. Sel. Top. Appl., 8, 4442–4459, 2015.

Roy, A., Toose, P., Williamson, M., Rowlandson, T., Derksen, C., Royer, A., Berg, A., Lemmetyinen, J., and Arnold, L.: Response of L-Band brightness temperature to freeze/thaw and snow dynamics in a prairie environment, Remote Sens. Environ., 191, 67–80, 2017.

Schwank, M., Mätzler, C., Wiesmann, A., Wegmüller, U., Pulliainen, J., Lemmetyinen, J., and Drusch, M.: Snow density and ground permittivity retrieved from L-band radiometry: A synthetic analysis, IEEE J. Sel. Top. Appl., 8, 3833–3845, 2015.

Skou, N., Misra, S., Balling, J. E., Kristensen, S. S., and Sobjaerg, S. S.: L-band RFI as experienced during airborne campaigns in preparation for SMOS, IEEE T. Geosci. Remote, 48, 1398–1407, 2010.